51

Converging three-dimensional Stokes flow of two fluids in a T-type bifurcation

By JOSEPH ONG, GIORA ENDEN†
AND ALEKSANDER S. POPEL

Department of Biomedical Engineering, School of Medicine, The Johns Hopkins University,
Baltimore, MD 21205 USA

Studies of three-dimensional Stokes flow of two Newtonian fluids that converge in a T-type bifurcation have important applications in polymer coextrusion, blood flow through the venous microcirculation, and other problems of science and technology. This flow problem is simulated numerically by means of the finite element method, and the solution demonstrates that the viscosity ratio between the two fluids critically affects flow behaviour. For the parameters investigated, we find that as the viscosity ratio between the side branch and the main branch increases, the interface between the merging fluids bulges away from the side branch. The viscosity ratio also affects the velocity distribution: at the outlet branch, the largest radial gradients of axial velocity appear in the less-viscous fluid. The distribution of wall shear stress is non-axisymmetric in the outlet branch and may be discontinuous at the interface between the fluids.

1. Introduction

Theoretical and experimental study of two immiscible fluids converging in three-dimensional bifurcations is relevant to a wide variety of disciplines, ranging from polymer coextrusion and reservoir engineering to biofluid mechanics. The problem of blood flow in venules is the primary motivation for the present study. Blood acts to transport oxygen and nutrients to tissues and remove waste products from tissues. Within living tissues, blood is transported via a microvascular network of arterioles, capillaries, and venules. Most of the resistance to blood flow occurs at the microvascular level. A significant part, typically 15–20%, of the total microvascular resistance occurs in the venules. Venular resistance is known to vary in concert with arteriolar resistance and inversely with blood flow. Changes in venular resistance with flow are crucial for maintaining capillary blood pressure within a certain range and, therefore, for maintaining fluid balance. Some of the resistance changes are attributed to rheological effects of red blood cell aggregation, but the investigation of this and other mechanisms is still in progress (e.g. Marshall 1991).

In addition to its role in venular resistance changes, the pattern of blood flow in venular networks is important for understanding the distribution of platelets, which are essential for blood clotting (Tangelder *et al.* 1985; Sato & Ohshima 1989; Oude Egbrink *et al.* 1991), and white blood cells, which are particularly important during inflammation (House & Lipowsky 1988). The microvascular network can be modelled, to a first approximation, as vascular segments of circular cross-section linked in binary fashion to form bifurcations. Understanding blood flow regulation and transport

† Author to whom correspondence should be addressed.

phenomena in the microcirculation requires quantitative knowledge of flow in individual microvascular bifurcations.

To date, most experimental and theoretical studies of blood flow in microvascular bifurcations have concentrated on diverging arteriolar bifurcations in order to understand and quantify phase separation between plasma and red cells (Schmid-Schönbein *et al.* 1980; Pries *et al.* 1989, 1990; Yan, Acrivos & Weinbaum 1991; Enden & Popel 1992, 1994). In arterioles, hydrodynamic interactions of red cells with the walls result in a marginal cell-free layer of plasma and a core of concentrated suspension of red cells (Schmid-Schönbein *et al.* 1980; Pries *et al.* 1989; Yamaguchi, Yamakawa & Niimi 1992). The non-uniform distribution of red cells at the inlet cross-section of the main branch leads to non-uniform distribution of these cells into the branches of the arteriolar bifurcation. Owing to the small diameters and velocities involved, the Reynolds number, *Re*, is smaller than unity and, therefore, theoretical models pertinent to flow problems in the microcirculation use the Stokes flow approximation.

Owing to phase separation in arteriolar networks, the volumetric concentration of red cells in the blood, called the haematocrit, is distributed unevenly within capillary networks. As a result of this heterogeneity, branches of converging venular bifurcations may carry blood of different haematocrit into the collecting vessel. When two streams of venular blood with different haematocrits converge, the streams tend to retain their original haematocrit without significant mixing until the next bifurcation is reached, because the diffusion of red cells across the interface between the streams is extremely slow (Schmid-Schönbein & Zweifach 1975; Carr 1989). Since blood viscosity is known to increase with haematocrit and red cell aggregation (Lipowsky, Usami & Chien 1980), the converging streams of blood may have different viscosities. As a first approximation, the two streams of blood entering from the two branches are modelled here as immiscible Newtonian fluids with different viscosities.

The aim of this work is to provide a quantitative solution to the problem of steady two-component Stokes flow in a three-dimensional converging bifurcation. The viscosity ratio, μ^*, between the inlet streams is varied between 0.125 and 8 to evaluate its effect on the fluid mechanics of the problem. The chosen values for μ^* also reflect the realistic range of viscosities at a venular bifurcation; this ratio may reach even lower or higher values, depending upon haematocrits and degrees of red cell aggregation in the merging streams. The calculations are performed for a single value of side-to-main-branch radius ratio $R^* = 0.4$, and for a range of side-to-outlet-branch flow ratios, $Q^* = 0.1–0.9$.

To our knowledge, the problem of two fluids with different viscosities converging in a three-dimensional bifurcation has not been studied theoretically or experimentally, and this is the first attempt at a solution without knowing *a priori* the shape of the interface separating the fluids. The solution presented is only a first approximation to flow in venular bifurcations, since blood exhibits non-Newtonian shear-dependent viscosity, resulting mainly from formation of red cell aggregates. In future studies, converging flows of non-Newtonian fluids with non-uniform distribution of haematocrit at the inlet branches will be considered. Owing to the particulate nature of blood, the results should be interpreted with caution when applied to very small venules where red blood cell size becomes comparable to vessel diameter. The results may also be applicable to converging streams in arteriolar bifurcations of arcade networks.

2. Mathematical model and method of solution

2.1. *Assumptions and simplifications*

The flow problem to be modelled involves two homogeneous Newtonian fluids with different viscosities that converge at a three-dimensional T-type bifurcation of rigid circular cylinders. Steady flow is assumed, and the two fluids are modelled as immiscible. Surface tension and inertia are neglected. The main branch is aligned with the y-axis and the side branch runs along the z-axis, forming a 90° bifurcation as shown in figure 1. The walls of both branches intersect at a sharp edge. We choose not to smooth out the edge to avoid introducing additional geometrical parameters into the problem.

2.2. *Variables and parameters*

Denote the volumetric flow rate Q_i, radius R_i, and viscosity μ_i, at the inlet of the main branch, $i = 1$, and side branch, $i = 2$. Flow is non-dimensionalized with respect to $Q_{out} = Q_1 + Q_2$, lengths with respect to R_1, and viscosities with respect to μ_1. The following quantities are defined:

$$Q^* = Q_2/Q_{out}, \quad R^* = R_2/R_1, \quad \mu^* = \mu_2/\mu_1.$$

Dimensionless velocity, u, is expressed in terms of its Cartesian components (u, v, w), and non-dimensionalized with respect to $2\bar{U}_{out}$, where $\bar{U}_{out} = Q_{out}/(\pi R_1^2)$ is the dimensional mean velocity at the outlet. Pressure, p, is non-dimensionalized with respect to $2\mu_1 \bar{U}_{out}/R_1$. Unless specified otherwise, all parameters and variables hereinafter appear in dimensionless form.

2.3. *Geometrical and flow parameters*

The following geometrical parameters are chosen: total length of the main branch equals 8; length of the side branch, measured from the centre of the side branch inlet to the midpoint of the main branch axis, equals 4, and side-to-main branch radius ratio, R^*, equals 0.4. Numerical calculations have shown that lengthening the branches further does not affect the flow regime within the computational domain. In this study, flow ratios are $Q^* = 0.1, 0.2, 0.3, 0.4, 0.5, 0.6, 0.7, 0.8, 0.9$; viscosity ratios are $\mu^* = 0.125, 0.25, 1, 4, 8$.

2.4. *Numerical procedure*

The non-dimensional Stokes equations become

$$-\nabla p_1 + \nabla^2 u_1 = 0, \quad -\nabla p_2 + \mu^* \nabla^2 u_2 = 0 \tag{1}$$

for fluids 1 and 2, respectively.

At both inlets of the bifurcation, parabolic velocity profiles are imposed, and the no-slip boundary condition is specified at the walls. Velocity and tangential stress are continuous at the interface between the fluids. At the outlet cross-section the stress-free boundary condition is specified, i.e. the normal component of stress is set to zero. This latter boundary condition does not necessarily imply that flow in the outlet branch is fully developed. Indeed, a number of experimental and theoretical studies indicate that two-component stratified flow in a circular tube may gradually evolve to a concentric axisymmetric arrangement in which the more-viscous fluid forms a core, and the less-viscous fluid occupies the peripheral annular layer (Everage 1973; MacLean 1973; White & Lee 1975; Williams 1975). However, evidence exists that such a transition region is very long and may extend over tens or hundreds of tube diameters. The stress-free boundary condition at the outlet separates the bifurcation region, where the
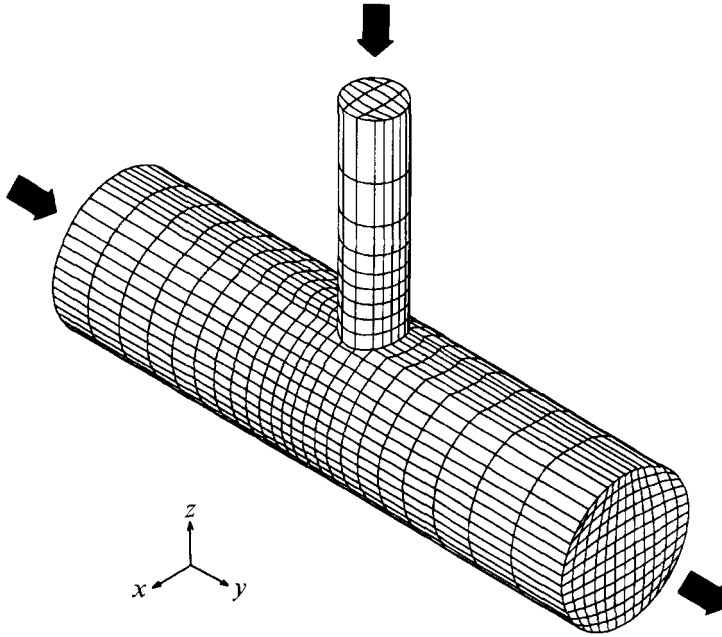
FIGURE 1. The finite element mesh consisting of 3474 27-node isoparametric bricks and the coordinate system with origin at the centre of the main branch axis.

interface undergoes rapid changes, from the long straight tube, where interface evolution is slower. The problem of the slower interface evolution to its fully developed shape is beyond the scope of the present study.

To impose the condition of fluid immiscibility, viscosity is modelled as a function of a parameter C, referred to as concentration, which is assumed to be conserved within fluid particles. Hence, for steady flow the material derivative DC/Dt vanishes such that

$$(u \cdot \nabla) C = 0. \tag{2}$$

Solving (1) and (2) with boundary conditions $C = C_1$ at the main branch inlet and $C = C_2$ at the side branch inlet is, therefore, equivalent to the condition of immiscibility. For a concentration-dependent viscosity, $\mu(C)$, equations (1) are equivalent to

$$-\frac{\partial p}{\partial x_j} + \frac{\partial}{\partial x_k} \mu(C) \left(\frac{\partial u_k}{\partial x_j} + \frac{\partial u_j}{\partial x_k} \right) = 0, \quad j, k = 1, 2, 3 \tag{3}$$

in Cartesian tensor notation. Viscosity is chosen as

$$\mu = \begin{cases} 1 & \text{for} \quad C < \bar{C} \\ \mu^* & \text{for} \quad C \geqslant \bar{C} \end{cases} \tag{4}$$

where $\bar{C} = \frac{1}{2}(C_1 + C_2)$ is the average concentration.

This approach can be generalized to treat converging flow of two suspensions with different concentrations of suspended particles when the particles diffuse with a diffusion coefficient D_p. In this case, (2) should be modified by adding a diffusion term $\nabla D_p \nabla C$ to the right-hand side. The problem may then be solved by using the numerical approach of the present study.

With use of the finite element program FIDAP (Fluid Dynamics International, Evanston, IL), the geometrical domain is discretized into brick elements, and the discrete version of (2) and (3) is solved for the global vector of unknowns

$V = (u, p, C)$ via the Galerkin method. Velocity components are calculated at the element nodes, whereas pressure is calculated at the centre of the elements.

This procedure yields a large system of nonlinear algebraic equations. A segregated algorithm is used to decompose the system into a set of decoupled sub-matrix systems. Pressure is used to satisfy the continuity equation. The pressure-projection version of the segregated algorithm is employed to obtain an explicit matrix equation for pressure. A conjugate-gradient-based method is used to solve the decoupled systems iteratively. Convergence is achieved when the relative error for each variable is less than 0.001.

2.5. *Computational strategy*

Initial computations were performed on a CRAY Y-MP supercomputer, and the final numerical solution was obtained using a Silicon Graphics POWER Series 4D380VGX computer equipped with 96 megabytes of random-access memory.

We checked the accuracy of the proposed technique by simulating the developing flow of two fluids in an axisymmetric core–annulus configuration through a straight tube. The nodal arrangement and density in this problem are similar to that of the bifurcation problem. By specifying inlet interface position, fluid viscosity, and inlet parabolic velocity profile, the fully developed downstream interface position may be calculated analytically. Computational results for a variety of viscosity ratios of interest in this study show less than 1% error. Additionally, numerically calculated total fluid flux at the outlet shows less than 1% deviation from the imposed flux at the inlet.

For the bifurcation problem, the computational domain is discretized as illustrated in figure 1. The problem is solved in a series of computational stages. First, a low-density mesh consisting of 15632 8-node isoparametric brick elements (17805 nodes) is used. Equation (3) is solved with the assumption of equal viscosity, i.e. $\mu^* = 1$. This first stage provides an initial guess for velocity and pressure to be used in further calculations. Second, the convection–diffusion problem governed by (2) is solved by using the same low-density mesh to obtain an initial guess for concentration. Third, these initial guesses are used in solving (2) and (3) simultaneously on a higher-density mesh consisting of 68896 8-node isoparametric brick elements (74585 nodes). This solution provides an initial guess for solving (2) and (3) with a different low-density mesh consisting of 3474 27-node isoparametric brick elements (31013 nodes). Numerical experiments show that calculations involving 8-node elements require much less computational time and resources than those involving 27-node elements, but they are less accurate. The 27-node element mesh enables the acquisition of a more accurate solution with less than half the nodes of the high-density 8-node element mesh. Relaxation factors for velocity, pressure, and concentration, as well as an upwinding factor for the concentration, are selected empirically.

Even though (2) does not contain a diffusion term, 'numerical diffusion' is present in a narrow transition region where concentration varies between C_1 and C_2. The interface between the fluids is identified by tracing the contour $C = \bar{C}$. This procedure provides a numerically stable interface, i.e. the interface is insensitive to small variations of the computational mesh. The method of identifying interface shape has been compared to a different method (Enden & Popel 1992), where massless 'marker' particles initially located near the walls of the branches are traced along their respective trajectories until they intersect the outlet cross-section. Trajectories, or streamlines, originating at the inlet of the main branch practically merge with those arriving from the side branch, thereby outlining the interface.

Figures 2(a) and 2(b) illustrate how streamlines trace the fluid interface. Figure 2(a)
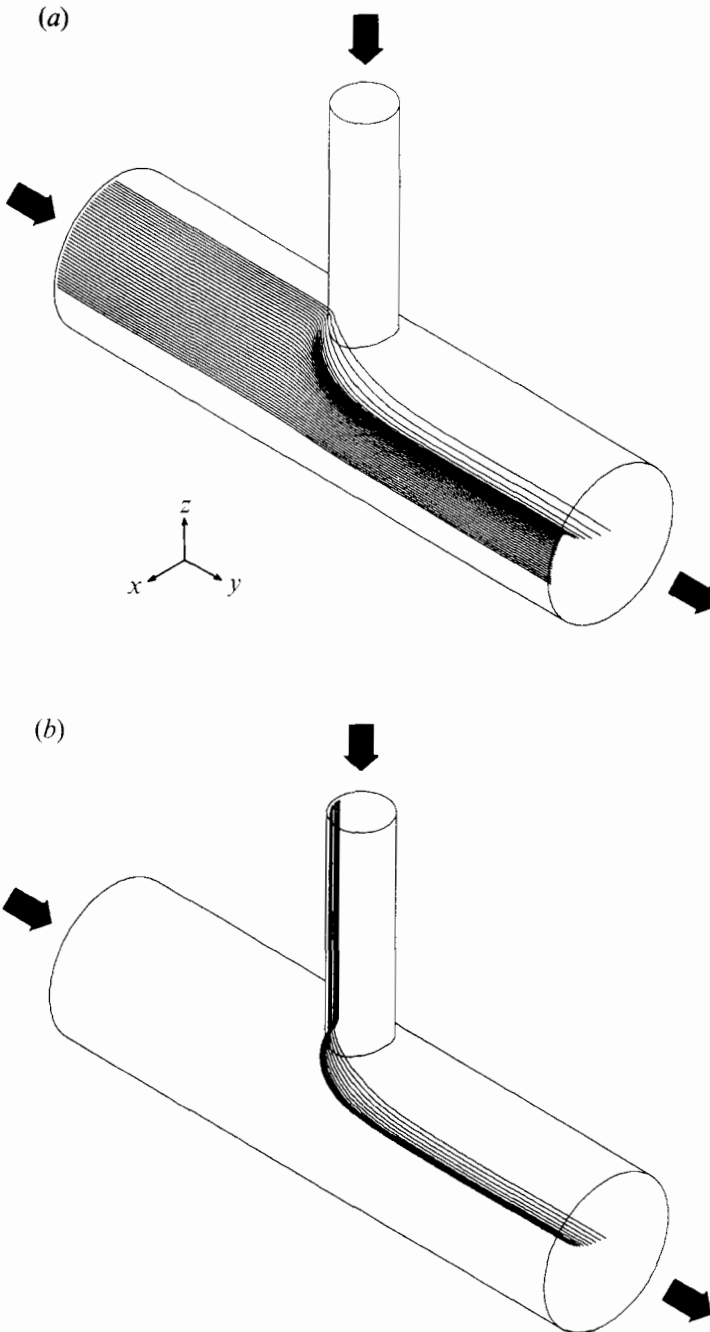
(*a*)

(*b*)

FIGURE 2. Streamlines originating near the walls: (*a*) at the inlet cross-section of the main branch, (*b*) at the inlet cross-section of the side branch. Heavy arrows indicate flow direction. $R^* = 0.4$; $Q^* = 0.4$; $\mu^* = 0.25$. Note that an approximation of the interface is traced out at the outlet cross-section.

shows 40 streamlines originating at $0.95R_1$ radially and evenly spaced at the main-branch inlet. Upstream of the bifurcation in the main branch all streamlines remain straight, reflecting fully developed Poiseuille flow. Directly at the bifurcation, however, streamlines originating closest to the top of the main branch bend sharply, while those
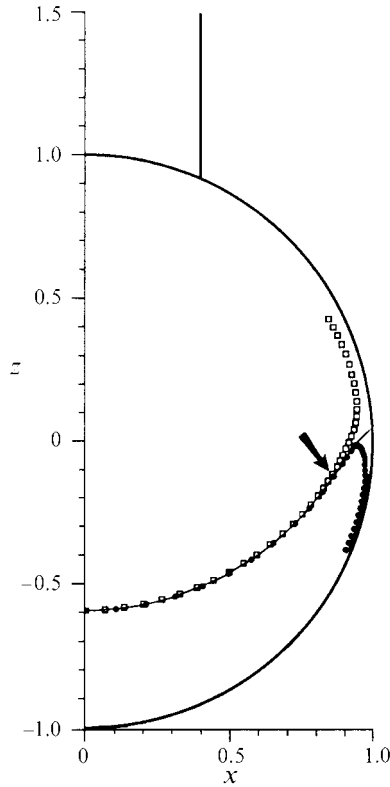
FIGURE 3. Superposition of streamlines originating near the wall at the inlet of the main branch (solid symbols) and of the side branch (open symbols) and the average-concentration contour (solid line) at the outlet cross-section. To the right of the arrow the streamlines diverge and do not follow the interface. $R^* = 0.4$; $Q^* = 0.8$; $\mu^* = 4$.

originating near the main branch sides remain relatively straight. At the bifurcation, inlet flow from the side branch causes downward bending of all main branch streamlines. Similarly, figure 2(*b*) shows 15 streamlines originating at $0.95R_2$ radially and evenly spaced at the side-branch inlet. Again, the streamlines remain straight until the bifurcation is encountered, at which point the streamlines initially bend toward the main-branch inlet and eventually head toward the main-branch outlet.

Of primary importance is determining how the interface intersects the outlet cross-section. The shape of this curve provides information about the cross-sectional area occupied by fluid originating from a particular branch. Fluid above the interface originates from the side branch, whereas fluid below the interface originates from the main branch. Figure 3 shows excellent agreement between the trajectories method and the concentration method up to the point marked by the arrow. The particle trajectory method is inaccurate for particles containing radial velocity components close to the walls. The slightest radial component near the wall will send that particle to the wall; this phenomenon is readily seen at high flow ratio, Q^*. Although both techniques are sufficiently accurate up to a certain distance from the wall, the concentration method has the advantage of approximating the interface up to the wall. Thus, the concentration method is used consistently in the present study.

3. Results and discussion

We now describe the relevant characteristics of the solution to the flow problem: the shape of the interface between the fluids, the velocity and pressure distributions, and the distribution of wall shear stress.

3.1. *Fluid interface geometry*

The flow ratio and viscosity ratio are important parameters which affect the shape of the interface between the two fluids. Figure 4(a) demonstrates the effect that varying the flow ratio has on interface shape at the outlet cross-section when the viscosity ratio, μ^*, is 0.25: for this viscosity ratio, the outlet velocity profiles are non-parabolic. As flow from the side branch increases, the interface bulges away from the side branch. Overall interface shape is similar for each Q^* investigated: low slope near the symmetry plane and continuously steeper slope approaching the wall. A similar feature was found in a previous study (Enden & Popel 1992) for $\mu^* = 1$ and $R^* < 1$. However, in that study it was found that for $R^* = 1$ and small values of Q^*, the interfaces bulge slightly toward the side branch. Interestingly, for a given μ^* the interfaces do not appear to intersect as Q^* is varied.

In addition to changes in the flow ratio, the interface shape is strongly influenced by the viscosity ratio, as shown in figure 4(b). As μ^* increases for a given Q^*, the interface bulges further away from the side branch, the intersection of the interface with the walls shifts toward the side branch, and the slope of the interface near the wall increases. As figure 4(b) indicates, the lower-viscosity fluid tends to envelop the higher-viscosity fluid, thereby reducing the wall surface in contact with the higher-viscosity fluid. In §3.5 it will be shown that this may lead to a decrease in flow resistance in the outlet branch.

3.2. *Velocity distribution*

The velocity and pressure distributions throughout the bifurcation are also strongly affected by the viscosity ratio. The effect of the viscosity ratio on the velocity field in the bifurcation region is evident in the symmetry plane shown in figure 5. Vectors indicating velocity magnitude and direction are plotted at each nodal point in the symmetry plane. A solid line representing the interface originates at the stagnation point (located at the top of the main branch immediately upstream of the bifurcation) and extends to the outlet. When the flow is presented from this perspective, major differences in downstream velocity profile are observed for different viscosity ratios. For all cases, parabolic velocity profiles are maintained upstream of the bifurcation in both the main and side branches, but at the bifurcation the velocity field adjusts in accordance with viscosity differences. Figure 5 shows that maximum velocity at the outlet branch is reached in the fluid with lower viscosity. The existence of a stagnation point in a similar flow of a homogeneous viscous fluid was pointed out in an earlier numerical study by Tutty (1988). He studied flow from semi-infinite space into a small side branch and discovered a stagnation point downstream from the branch. Since Stokes flow is reversible, his solution is similar to the present analysis for $\mu^* = 1$, but for two converging streams the stagnation point would be upstream from the bifurcation, in agreement with the present results.

The outlet velocity distribution is highly dependent on viscosity ratio, as demonstrated by figure 6. To display these distributions, we interpolate the velocity profiles onto a regular grid. The solid arc in the (x, z)-plane represents the wall of the outlet, while the heavy line on the surface is the fluid interface. For $\mu^* = 1$ (figure 6b) the velocity profile is parabolic; however, $\mu^* \neq 1$ (figure 6a, c) is characterized by
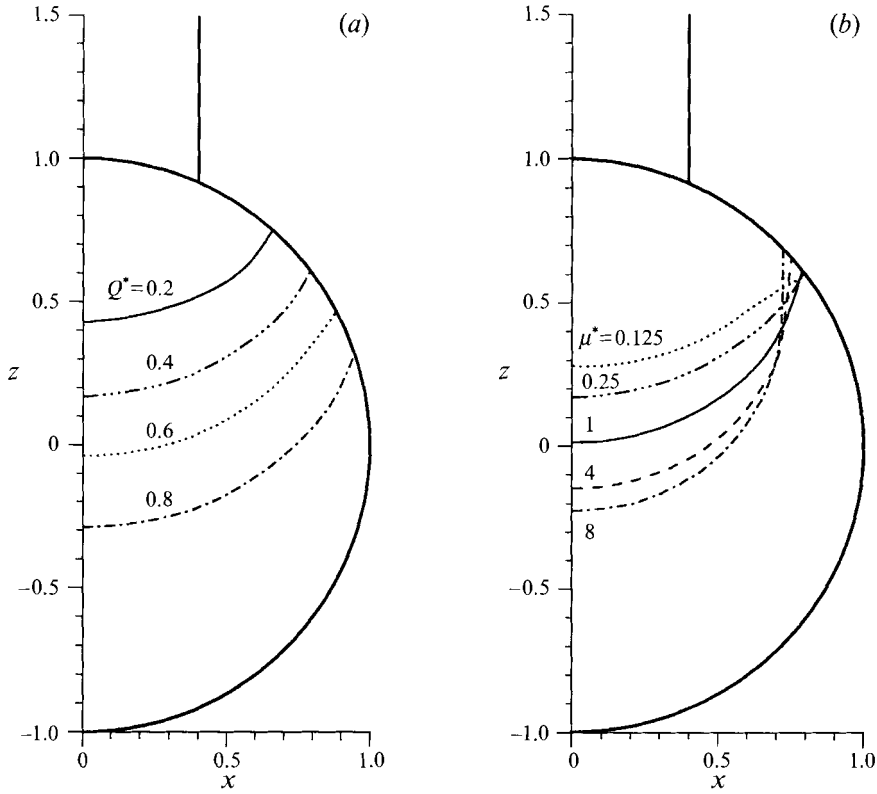
FIGURE 4. The interface at the outlet cross-section for (a) $Q^* = 0.2$, 0.4, 0.6, 0.8; $\mu^* = 0.25$; (b) $\mu^* = 0.125$, 0.25, 1, 4, 8; $Q^* = 0.4$. $R^* = 0.4$.

asymmetric velocity profiles in which radial velocity gradients are higher in the less-viscous fluid. The accuracy of the results is checked by comparing the flow ratio imposed by the boundary conditions with the flow ratio calculated by integration at the outlet. The relative difference between the computed and the specified flow ratios is less than 1%.

3.3. Pressure distribution

Fully developed Poiseuille flow exists upstream from the bifurcation in the main branch. In dimensional variables, volumetric flow rate, Q_1, can be expressed in terms of pressure gradient, $\partial P/\partial Y$, in the form of Poiseuille's law as

$$Q_1 = \frac{\pi R_1^4}{8\mu_1}\left(-\frac{\partial P}{\partial Y}\right). \tag{5}$$

Expressing $\partial P/\partial Y$ from (5), we obtain after non-dimenionalization

$$-\left(\frac{\partial p}{\partial y}\right) = 4(1 - Q^*). \tag{6}$$

Therefore, the dimensionless upstream pressure gradient in the main branch is only a function of flow ratio. Figure 7(a) shows the numerical results of the pressure distribution along the y-axis for viscosity ratios 0.125, 0.25, 1, 4, and 8. In this figure the flow ratio $Q^* = 0.4$, so (6) gives a normalized pressure gradient of 2.4. All slopes between $y = -4$ and -1 in figure 7(a) agree with this value to within 1%. Actual pressure values within this range are monotonically increasing with viscosity ratio.
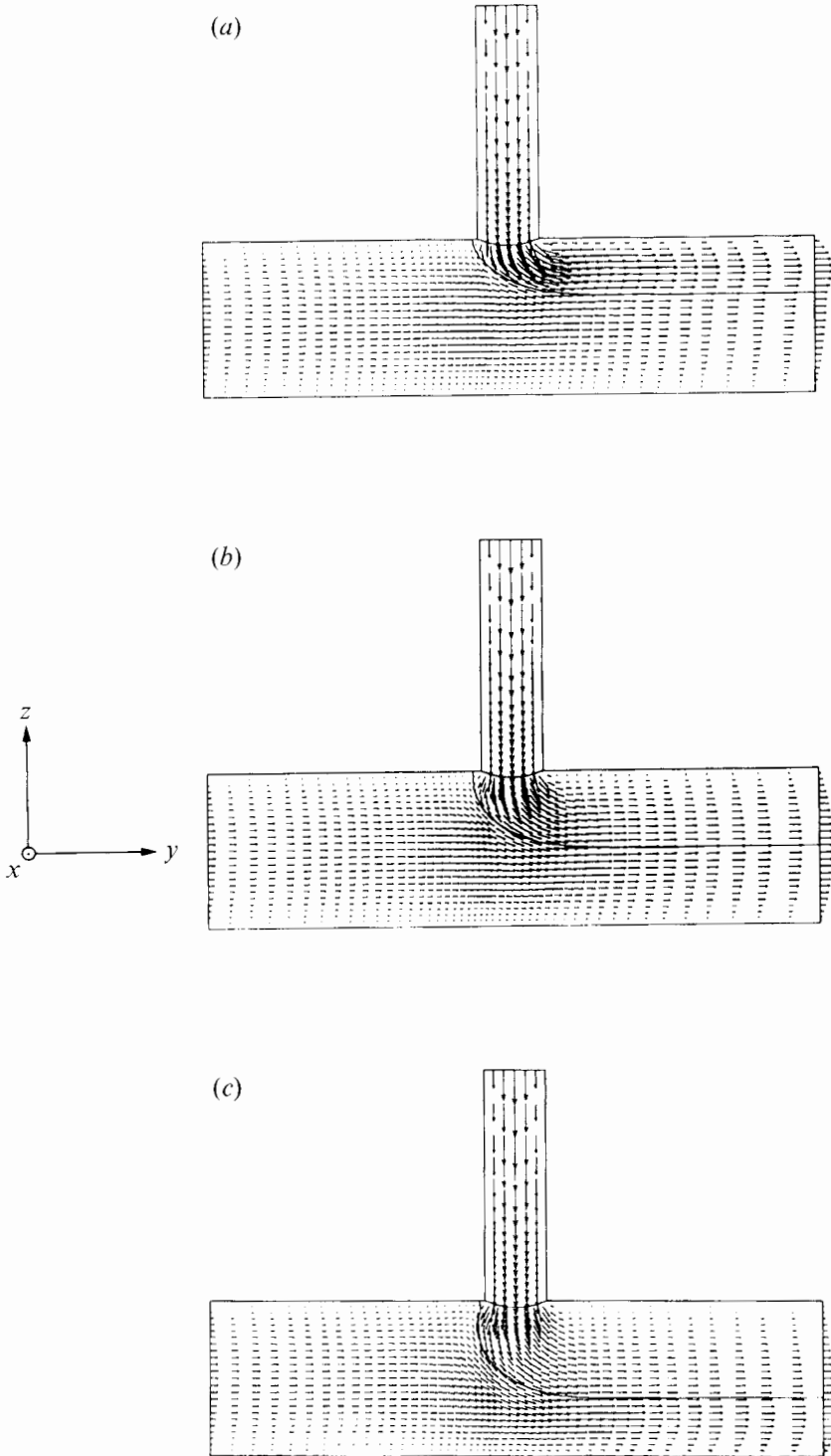
J. Ong, G. Enden and A. S. Popel

FIGURE 5. Superposition of velocity field and interface at the (y, z)-symmetry plane:
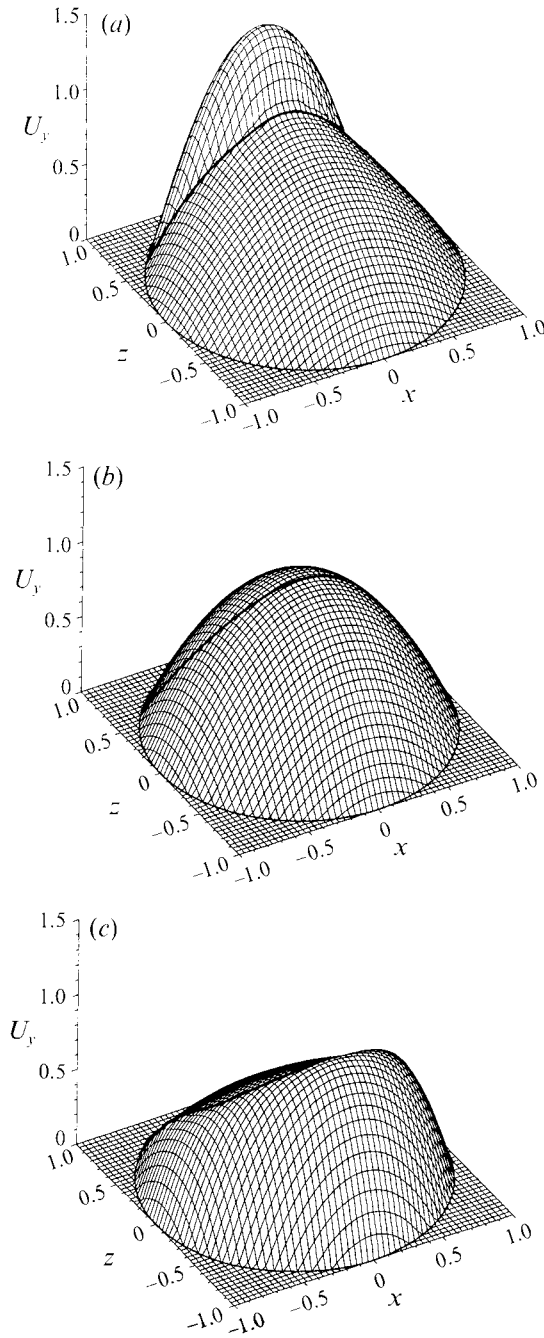(a) $\mu^* = 0.125$, (b) 1, (c) 8. $R^* = 0.4$; $Q^* = 0.4$.

FIGURE 6. Three-dimensional velocity profiles at the outlet cross-section: (a) $\mu^* = 0.125$, (b) 1, (c) 8. The interface is marked by a thick line. $R^* = 0.4$; $Q^* = 0.4$.

Note that the stress-free boundary condition imposed at the outlet branch yields practically zero pressure at the outlet cross-section, since the axial derivative of velocity at the outlet is negligible.

At the bifurcation, the pressure gradient changes smoothly within a transition region $-1 \leqslant y \leqslant 1$. Some flattening of the slope is present around $y = -0.4$ for $\mu^* > 1$. For

3

J. Ong, G. Enden and A. S. Popel

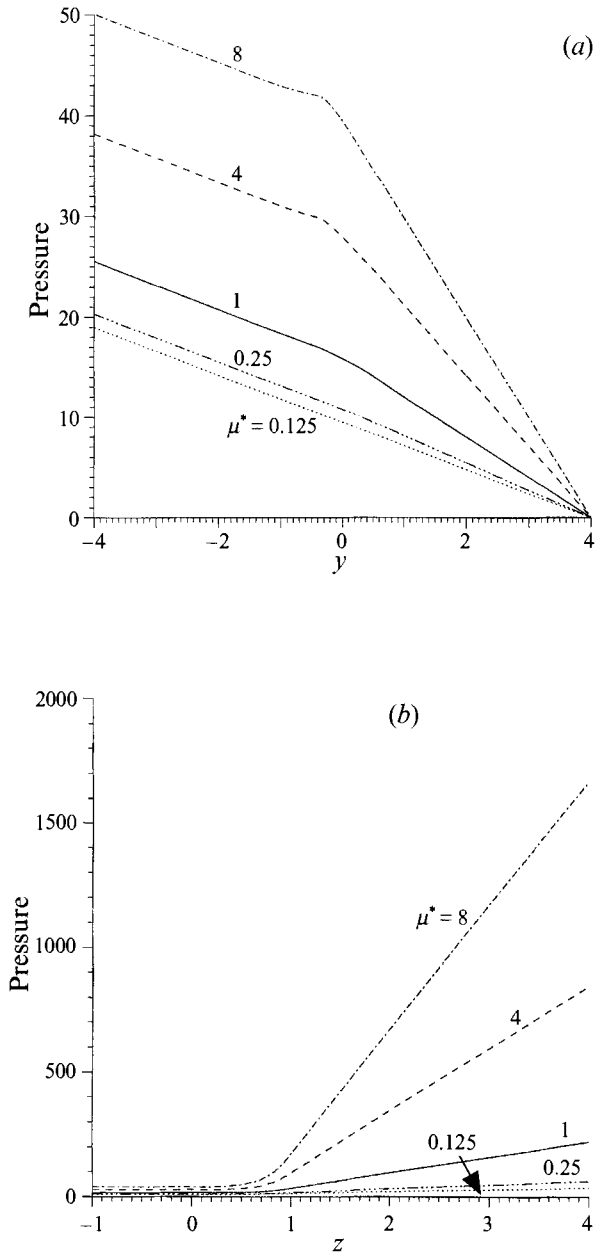FIGURE 7. Normalized pressure distribution for $R^* = 0.4$, $Q^* = 0.4$, and different values of μ^*: (a) along the main-branch axis; (b) along the side-branch axis.

the region $1 \leqslant y \leqslant 4$ the pressure distribution along the axis becomes linear again but with a different slope. The slopes of these profiles are not described by Poiseuille relationships, since flow in the outlet branch is stratified (this issue is discussed in §3.5). A similar analysis can be made for the side branch. The volumetric flow rate in the side branch is

$$Q_2 = \frac{\pi R_2^4}{8\mu_2}\left(\frac{\partial P}{\partial Z}\right), \tag{7}$$

and the non-dimensional pressure gradient becomes

$$\frac{\partial p}{\partial z} = \frac{4\mu^*Q^*}{(R^*)^4}.$$ (8)

In figure 7(b) the numerical results for $z > 1$ agree with analytical results that correspond to Poiseuille flow to within 1%. Pressure values remain approximately constant between $z = -1$ and 0.2, yielding zero slope for all viscosity ratios. In the range $0.2 < z < 1$, the slopes change smoothly with no discontinuity.

The accuracy of the above results is not affected by the singularity of pressure at the intersection edge. Indeed, Dagan, Weinbaum & Pfeffer (1982) and Tutty (1988) show analytically that, for flow of a homogeneous fluid into a pore, pressure becomes singular at the sharp edge. However, this singularity is local, and its effect decays rapidly beyond the edge.

3.4. Wall shear stress distribution

The numerical solutions show that the viscosity ratio has a significant effect on the wall shear stress distribution. Plotted in figure 8 is the magnitude of the non-dimensional wall shear stress (tangential component of the total stress at the wall), $|\tau_w|$, versus y for $Q^* = 0.4$. Wall shear stress is non-dimensionalized by $2\mu_1 \bar{U}_{out}/R_1$. In the inlet branches, sufficiently far from the bifurcation, the wall shear stress values are

$$\tau_1 = 2(1-Q^*), \quad \tau_2 = 2\mu^*Q^*/(R^*)^3.$$ (9)

The numerical results differ from (9) by less than 1%. Wall shear stress distributions for the main branch are shown along three lines parallel to the y-axis: $\theta = -90°$, $0°$, and $90°$ (figure 8a). At $\theta = 90°$, which is the line along the top of the main branch, $|\tau_w|$ is singular at the upstream and downstream corners of the side branch. No wall exists in the range $-0.4 < y < 0.4$; thus, wall shear stress is not displayed for this interval. There is a stagnation point upstream from the bifurcation, as seen in figure 5. A common feature at $\theta = 90°$ is an increase of $|\tau_w|$ from 1.2 to a maximum and then a decrease to zero at the stagnation point. The magnitude of this local maxima increases with μ^* (figure 8). Immediately downstream from the stagnation point, $|\tau_w|$ increases sharply, as indicated by the steep slope in the figure. This segment is a reflection of the τ_w curve with respect to the horizontal axis at the stagnation point. In fact, at the plane of symmetry, the only non-zero component of stress, τ_{yz}, changes sign at the stagnation point and decreases sharply toward the edge of the side branch. Similar behaviour of wall shear stress was demonstrated earlier in the problem of a single fluid drawn into a pore, where the magnitude of τ_w approaches infinity as the distance to the edge decreases (Tutty 1988). Distinct differences in $|\tau_w|$ downstream at $\theta = 90°$ are apparent between the higher and lower viscosity ratios. For $\mu^* < 1$, $|\tau_w|$ decreases smoothly from infinity at $y = 0.4$ to a constant value at the outlet. In addition, $|\tau_w|$ at the outlet is smaller than its inlet value of 1.2. For $\mu^* \geqslant 1$, however, $|\tau_w|$ is non-monotonic: initially it decreases and subsequently increases to a constant value greater than 1.2.

In contrast to the case $\theta = 90°$, along the lines $\theta = -90°$ and $0°$ the magnitude of wall shear stress $|\tau_w|$ is represented by a smooth curve, since these lines remain in the same fluid and no singularities are encountered along them. For $\mu^* = 1$ these two curves are nearly identical except near the bifurcation; the curves eventually merge to a constant value at the outlet, well within 1% of the exact value of 2, as shown in figure 8(c). At the outlet cross-section, τ_w is a function of θ when $\mu^* \neq 1$, as demonstrated in figure 8(a, b, d, e). Higher values of τ_w correspond to the more-viscous fluid. It is shown in the Appendix that if the interface intersects the wall in fully developed flow,
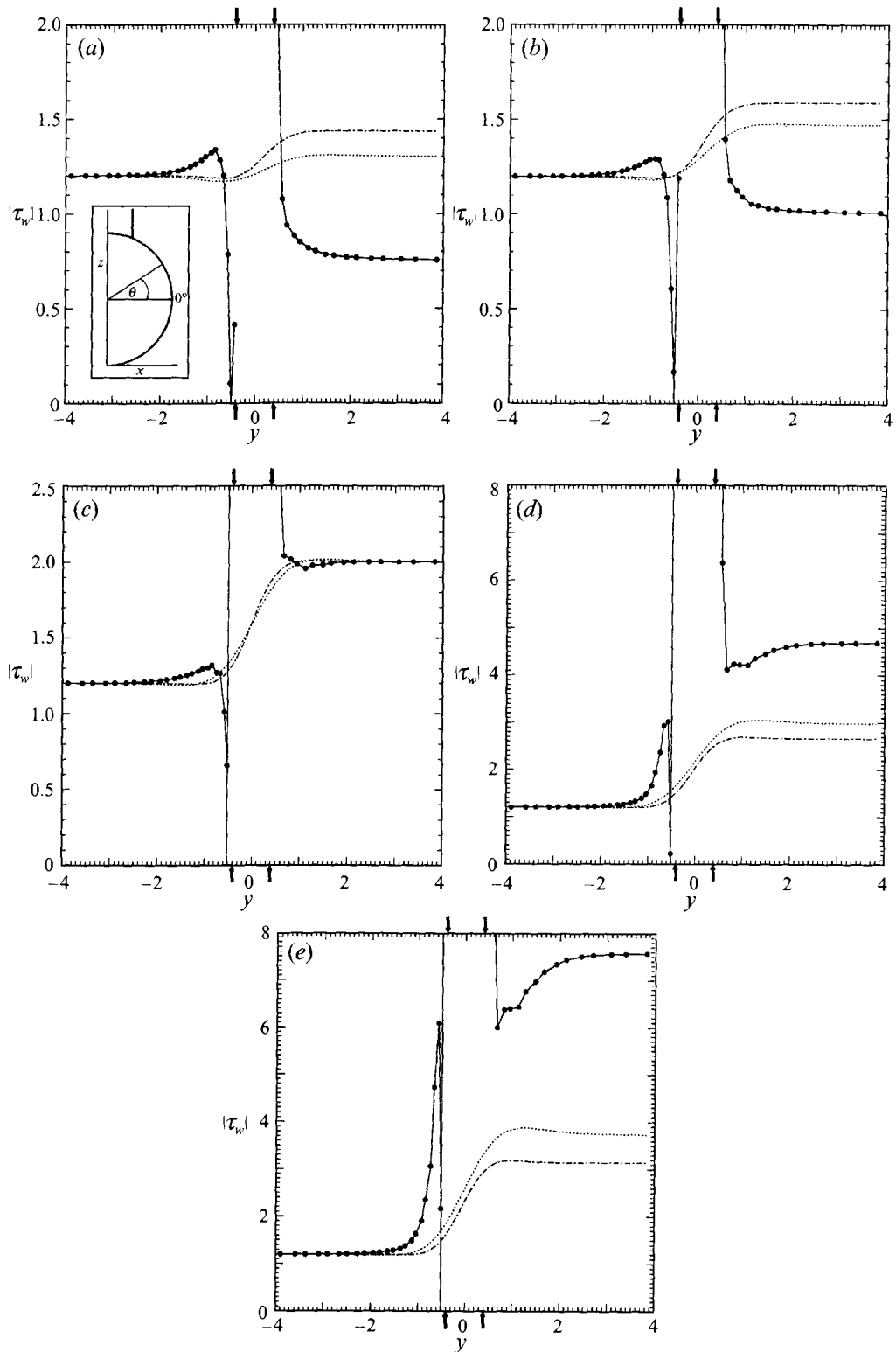
FIGURE 8. (*a*–*e*). For caption see facing page.

the intersection angle should be either $0°$ or $90°$, in the latter case τ_w is discontinuous and the ratio of the wall shear stress at the interface should equal the viscosity ratio, μ^*.

We now attempt to analyse the behaviour of τ_w near the interface. To increase numerical resolution close to the interface, an extremely dense mesh of the bifurcation consisting of 16896 27-node brick elements (127491 nodes) is utilized. Numerical results suggest discontinuous τ_w, as shown in figure 9 for $Q^* = 0.4$, and $\mu^* = 0.25$ and 4. These results illustrate the dependence of τ_w on θ at the outlet cross-section. The curve segment on the left represents the variation of τ_w along the wall in the fluid originating from the main branch, whereas the curve segment on the right represents τ_w in the fluid originating from the side branch, both calculated at the outlet cross-section. In both figures 9(a) and 9(b) the fluid with higher viscosity is responsible for the highest values of τ_w at the outlet cross-section. Extrapolation of the τ_w curve segments to the location where the interface contacts the wall suggests that at the interface $\tau_{w2}/\tau_{w1} \to \mu^*$.

Calculations of shear stress involve differentiation of the solution for velocity, and, therefore, accuracy near points of discontinuity is limited. Higher resolution of the curve segments shown in figure 9 in the neighbourhood of the interface would require a significantly denser mesh and additional computational efforts which have not been pursued. As for the angle of intersection between the interface and the wall, the computed interface does not appear to be normal to the wall (see figure 4b), contrary to the findings in the Appendix. This may be because the numerical solution of our calculations is of limited resolution very close to the wall, or because flow is not yet fully developed (discussed further in §3.6).

3.5. *Apparent viscosity of stratified flow at the outlet*

At the outlet, the flow is either changing very slowly or becomes fully developed and remains stratified. The relationship between volumetric flow rate, Q_{out}, and pressure gradient, $(\partial P/\partial Y)_{out}$, can be expressed in terms of apparent viscosity, μ_{app},

$$Q_{out} = \frac{\pi R_1^4}{8\mu_{app}} \left(-\frac{\partial P}{\partial Y} \right)_{out}, \tag{10}$$

or in dimensionless form as

$$\frac{\mu_{app}}{\mu_1} = \frac{1}{4} \left(-\frac{\partial p}{\partial y} \right)_{out}. \tag{11}$$

The outlet pressure gradient in (11) is determined numerically from the slope of axial pressure profiles in the main branch, shown in figure 7(a). It is useful to compare μ_{app} with an effective flow-weighted viscosity, μ_{eff},

$$\mu_{eff} = \frac{\mu_1 Q_1 + \mu_2 Q_2}{Q_{out}}. \tag{12}$$

In dimensionless form (12) is recast as

$$\frac{\mu_{eff}}{\mu_1} = 1 - Q^* + \mu^* Q^*. \tag{13}$$

FIGURE 8. The magnitude of wall shear stress, plotted along the $\theta = 90°$, $0°$, and $-90°$ lines, parallel to the y-axis: ——, $90°$; —·—·—, $0°$; ·····, $-90°$. Inset in (a) illustrates the definition of θ. (a) $\mu^* = 0.125$, (b) 0.25, (c) 1, (d) 4, (e) 8. $R^* = 0.4$ and $Q^* = 0.4$. For the $90°$ line, actual data points, represented by small filled circles, are connected with straight line segments. Small arrows above and below the graphs indicate the location of the side-branch walls.
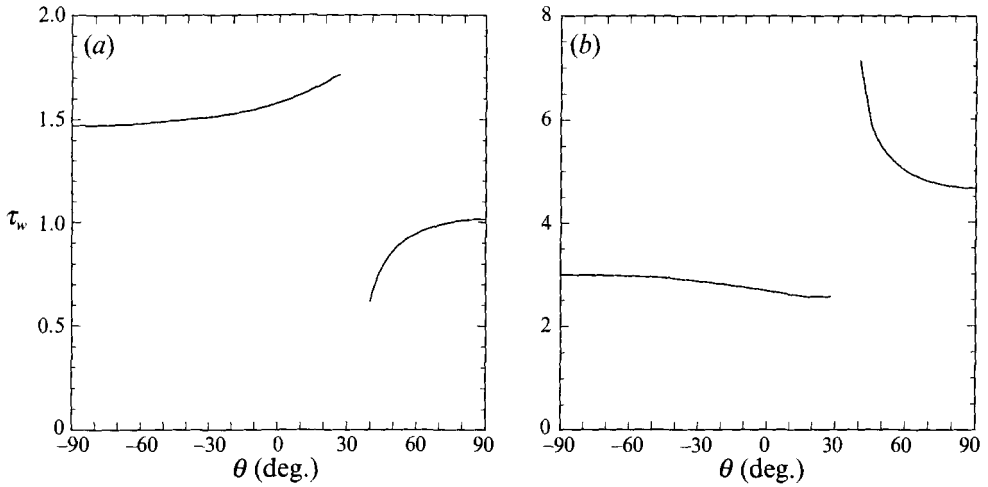
FIGURE 9. Wall shear stress plotted along the circumference at the outlet cross-section for (a) $\mu^* = 0.25$, (b) 4. $R^* = 0.4$ and $Q^* = 0.4$. The unit of the abscissa (degree) corresponds to that of figure 9a (inset).

In figure 10 the ratio μ_{app}/μ_{eff} is plotted versus flow ratio, Q^*, for viscosity ratios 0.125, 0.25, 4, and 8. Calculations are done in the range of flow ratio $Q^* = 0.1$–0.9. Surprisingly, the shapes of these curves are very similar to those of the corresponding upper and lower bounds calculated from the core–annulus configuration for a given Q^* and μ^*, which are denoted by thin solid lines. To find the upper and lower limits for μ_{app}/μ_{eff} consider the concentric fully developed flow of two fluids of different viscosities in a straight circular tube, such that: (i) the fluid with higher viscosity envelops that with the lower viscosity, and (ii) the fluid with lower viscosity envelops that with the higher viscosity. The representation of these curves can be calculated analytically as follows. Denote by μ_c and μ_p the viscosity of fluid in the core and at the periphery, respectively, and by Q_c and Q_p the flow of the fluid in the core and in the periphery, respectively. Denote

$$\lambda = \mu_p/\mu_c; \quad \phi = Q_p/(Q_c+Q_p); \quad \Delta = \phi[\lambda(1-\phi)+\phi].$$

The solution yields

$$\mu_{app}/\mu_{eff} = \lambda/[\lambda + 2(1-\phi)(\phi+\Delta^{\frac{1}{2}})(1-\lambda)(1+\Delta^{\frac{1}{2}})^{-2}].$$

For $\mu^* > 1$, the upper bound corresponds to $\lambda = \mu^*$, $\phi = Q^*$, and the lower bound to $\lambda = 1/\mu^*$, $\phi = 1-Q^*$. For $\mu^* < 1$, the upper bound corresponds to

$$\lambda = 1/\mu^*, \ \phi = 1-Q^*,$$

and the lower bound to $\lambda = \mu^*$, $\phi = Q^*$.

The general shape of the heavy solid curves in figures 10(a) and 10(b) is similar, as is the shape of the curves in figures 10(c) and 10(d). When $\mu^* = 1$, the ratio μ_{app}/μ_{eff} equals 1 (dotted line in figure 10). Notice that μ_{app}/μ_{eff} can be larger or smaller than unity depending on values of Q^* and μ^*, i.e. the resistance of the stratified flow can be larger or smaller than the flow resistance of a homogeneous fluid with viscosity μ_{eff}. It is evident that in the limits $Q^* \to 0$ and $Q^* \to 1$ only a single fluid would remain present in the outlet branch; thus, at $Q^* \to 0$ and $Q^* \to 1$, viscosity ratio $\mu_{app}/\mu_{eff} \to 1$ for any value of μ^*. This means that the curves shown in figure 11, if extended to the entire
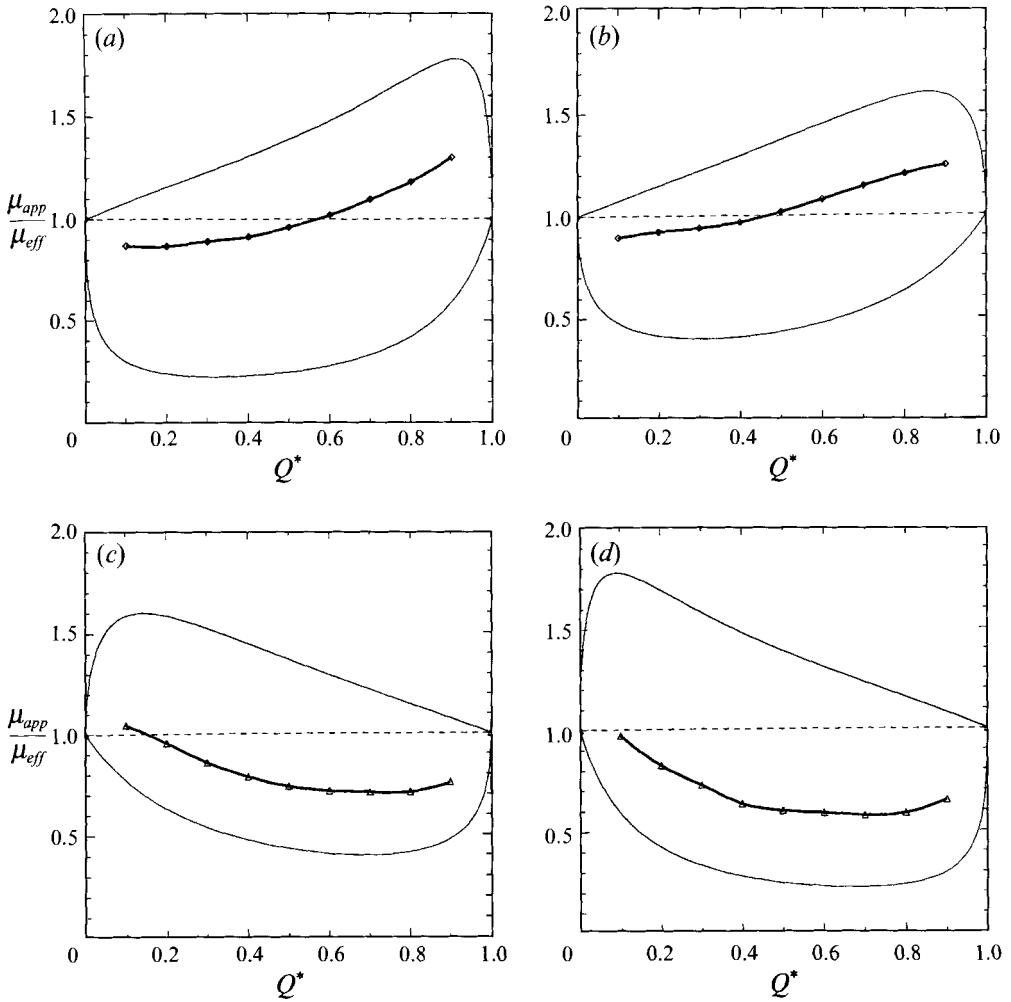
FIGURE 10. The ratio of apparent viscosity to effective viscosity, μ_{app}/μ_{eff}, plotted as a function of Q^* for (a) $\mu^* = 0.125$, (b) 0.25, (c) 4, (d) 8. $R^* = 0.4$. Calculated data points are shown as triangles or diamonds. Upper and lower bounds are indicated by a thin solid line.

range $0 \leqslant Q^* \leqslant 1$, would be non-monotonic as a function of Q^* and would have a minimum and a maximum. Equations (10) and (12) together with the results presented in figure 11 provide the relationship between volumetric flow rate and pressure gradient for these stratified flows. Alternatively, the hydrodynamic resistance per unit length is $8\mu_{app}/(\pi R_1^4)$. These may be considered as a generalization of Poiseuille's law for the above stratified flows.

In a number of cases, the behaviour of these curves can be qualitatively understood from the shape of the interfaces for different μ^*, as shown in figure 4(b). For $\mu^* > 1$, the more-viscous fluid enters the side branch and is enveloped by the less-viscous fluid from the main branch; the larger the value of μ^*, the smaller the wetting perimeter of the more-viscous fluid. This explains why most of the curve μ_{app}/μ_{eff} for $\mu^* = 4$ is below the value of unity. For $\mu^* < 1$ the reverse is not necessarily true since the interfaces remain concave, though to a lesser degree. Indeed, for $\mu^* = 0.25$ approximately half of the curve μ_{app}/μ_{eff} is above 1, whereas the other half is below 1.

3.6. *Possible evolution of the interface shape if the outlet is long*

A great many experimental and theoretical studies have been devoted to evaluation of the shape of the interface in two-component flow in a straight tube (Everage 1973; Southern & Ballman 1973; MacLean 1973; Joseph, Renardy & Renardy 1984; Joseph 1990). This problem is important in various technological applications, e.g. in oil flow through a pipeline with addition of a low-viscosity fluid to reduce the resistance to flow, or in stratified flow of two polymer melts through a tube in the process of spinning two-component fibres.

It has been shown experimentally that the less-viscous fluid tends to encapsulate the fluid with the higher viscosity, which tends to migrate into regions of lower shear rate (Joseph 1990). This relatively slow phenomenon conforms to the viscous-dissipation principle, which postulates that for a given flow, the amount of viscous dissipation is minimized. According to the variational method and the minimum viscous dissipation principle, the more-viscous fluid tends to concentrate at a circular core concentric with the tube, while the less-viscous fluid flows in an annular region between the core and the tube walls (Everage 1973; McLean 1973).

Theoretical three-dimensional analysis of the flow evolution of two immiscible fluids in a straight pipe is still unavailable. In fact, the problem of evolution of flow has been recently described by Joseph (1990) as follows: 'This difficult study is at best computationally intensive and at worst either too expensive or even beyond the capabilities of modern supercomputers'. Two-dimensional simulation of two-component flow in a channel which uses the lattice–gas automata technique showed that the fluid must traverse a length of 50–100 times the channel width before most of the more-viscous fluid forms a central core (Stockman, Stockman & Carrigan 1990). Another question about the two-component flow in a straight pipe is that if, indeed, an encapsulation occurs, what are the flow conditions for which the concentric core–annulus configuration is stable? This question has been addressed in studies using linear and nonlinear stability analyses (Joseph *et al.* 1984*b*; Joseph, Nguyen & Beavers 1984*a*; Chen & Joseph 1991). Useful results were obtained from the linearized stability theory where the stability criterion yielded an upper limit for the interface radius. For example, for a Reynolds number of 100 the linear stability analysis implied that the diameter ratio between the interface and the tube wall should be larger than 0.7 (Joseph *et al.* 1984*b*).

It is possible that in our numerical solution the velocity profile and, hence, the shape of the interface in the outlet branch are not fully developed. However, the rate at which the shape changes with distance may be negligible in comparison with the changes within the bifurcation region. It is also possible that the experimentally observed concentric stratification is inertial in nature; in other words it evolves at non-zero Reynolds numbers. In terms of applications to flow in venular bifurcations, the length of the outlet channel is sufficiently short, typically on the order of 10 diameters, and the flow is likely to remain stratified until the next bifurcation is encountered. In such a system, a very complex mixing pattern might result when flow passes through successive converging bifurcations.

4. Concluding remarks

In the present study, emphasis was placed on the effect of viscosity ratio, μ^*, while branch radius ratio was kept constant, $R^* = 0.4$, and flow ratio was varied, $Q^* = 0.1$–0.9. It is possible that for different values of parameters the qualitative

features of the flow are different from the ones described herein. It is known from previous calculations (Enden & Popel 1992) with $\mu^* = 1$ that for $R^* = 1$ the interface between the fluids originating from different branches may become nearly flat, in contrast to the shapes found in the present study. Additional studies are necessary to analyse this problem fully. As for applications to the venous microcirculation, this study provides the first theoretical results on blood flow in venular bifurcations. The three-dimensional flow velocity and shear stress distribution obtained will help in interpretation of experimental data on platelet and white blood cell distribution in the venular microcirculation. The study also provides an analogue of the Poiseuille law for stratified flow in a circular vessel. The calculated flow resistance (apparent viscosity) could differ by as much as 50% from the flow resistance of the corresponding homogeneous fluid. The resistance may be calculated as a function of flow ratio, viscosity ratio, and diameter ratio. In view of these results, conventional treatment of venular resistance using the Poiseuille law needs to be reassessed. Several important factors will have to be considered in the future. Among these are the non-Newtonian (shear-thinning and thixotropic) behaviour of blood resulting primarily from formation of red cell aggregates and the non-uniform distribution of haematocrit – particularly, the formation of cell-depleted layers of plasma near the walls. It should be pointed out that owing to the particulate nature of blood, the results presented here should be interpreted with caution when applied to very small vessels whose diameter is comparable to red blood cell size.

Appendix

Consider two-component fully developed flow in the vicinity of a circular arc with velocity $w(x, y)$ and an interface Γ as shown in figure 11. Let s be the local coordinate along the interface and n be the normal to the interface. The interface intersects the wall at an angle $90° - \alpha$. It will be shown that two cases are possible: (i) the interface is normal to the wall, $\alpha = 0°$, and the wall shear stress, τ_w, is discontinuous at the interface; (ii) the interface is tangential to the wall, $\alpha = 90°$, and the wall shear stress is continuous.

If the z-velocity component, w, is differentiable in both flow domains and at the walls, then from figure 12:

$$\frac{\partial w_i}{\partial s} = \frac{\partial w_i}{\partial x}\sin\alpha + \frac{\partial w_i}{\partial y}\cos\alpha, \tag{A 1}$$

$$\frac{\partial w_i}{\partial n} = -\frac{\partial w_i}{\partial x}\cos\alpha + \frac{\partial w_i}{\partial y}\sin\alpha, \tag{A 2}$$

where subscript $i = 1, 2$ denote fluids 1 and 2, respectively. Since $w = 0$ at the wall,

$$\frac{\partial w_1}{\partial x} \to 0, \quad \frac{\partial w_2}{\partial x} \to 0 \quad \text{as} \quad s \to 0. \tag{A 3}$$
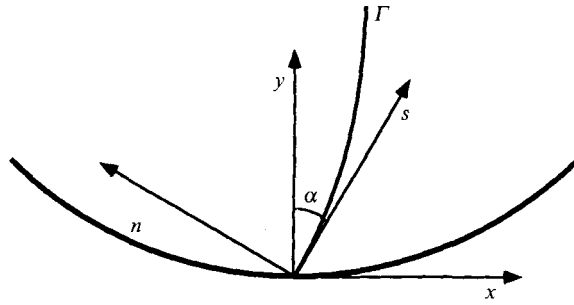
FIGURE 11. Schematic description of the interface intersecting the wall in a fully developed flow.

Velocity w is continuous at the interface; thus,

$$\frac{\partial w_1}{\partial s} = \frac{\partial w_2}{\partial s} \quad \text{on} \quad \Gamma. \tag{A 4}$$

Combining (A 1) with (A 3) and (A 4) yields

$$\left(\frac{\partial w_1}{\partial y} - \frac{\partial w_2}{\partial y}\right)\cos\alpha \to 0 \quad \text{as} \quad s \to 0. \tag{A 5}$$

Wall shear stresses in the fluids at the interface are expressed as

$$\tau_{w1} = \lim_{x \to +0} \mu_1 \frac{\partial w_1}{\partial y}, \quad \tau_{w2} = \lim_{x \to -0} \mu_2 \frac{\partial w_2}{\partial y}. \tag{A 6}$$

On the other hand, tangential shear stress is continuous at the interface, hence,

$$\mu_1 \frac{\partial w_1}{\partial n} \to \mu_2 \frac{\partial w_2}{\partial n} \quad \text{as} \quad n \to 0. \tag{A 7}$$

Combining (A 2) with (A 3) and (A 7) gives

$$\left(\mu_1 \frac{\partial w_1}{\partial y} - \mu_2 \frac{\partial w_2}{\partial y}\right)\sin\alpha \to 0 \quad \text{as} \quad s \to 0. \tag{A 8}$$

Equations (A 5) and (A 8) must be satisfied simultaneously. Two cases are possible: (i) $\alpha = 0°$, then (A 8) is satisfied, and from (A 5) it follows that $\partial w_1/\partial y = \partial w_2/\partial y$, or, using (A 6), at the interface

$$\tau_{w2} = \mu^* \tau_{w1}; \tag{A 9}$$

(ii) $\alpha = 90°$, then (A 5) is satisfied, and from (A 8) it follows that $\mu_1\, \partial w_1/\partial y = \mu_2\, \partial w_2/\partial y$, or $\tau_{w1} = \tau_{w2}$ at the interface.

REFERENCES

CARR, R. T. 1989 Estimation of haematocrit profile symmetry recovery length downstream from a bifurcation. *Biorheology* **26**, 907–920.

CHEN, K. & JOSEPH, D. D. 1991 Lubricated pipelining: stability of core-annular flow. Part 4. Ginzburg–Landau equations. *J. Fluid Mech.* **227**, 587–615.

DAGAN, Z., WEINBAUM, S. & PFEFFER, R. 1982 An infinite-series solution for the creeping motion through an orifice of finite length. *J. Fluid Mech.* **115**, 505–523.

ENDEN, G. & POPEL, A. S. 1992 A numerical study of the shape of the surface separating flow into branches in microvascular bifurcations. *J. Biomech. Engng* **114**, 398–405.

ENDEN, G. & POPEL, A. S. 1994 A numerical study of plasma skimming in small vascular bifurcations. *J. Biomech. Engng* **116**, 79–88.

EVERAGE, A. E. 1973 Theory of stratified bicomponent flow of polymer melts. I. Equilibrium Newtonian tube flow. *Trans. Soc. Rheol.* **17**, 629–646.

HOUSE, S. D. & LIPOWSKY, H. H. 1988 In vivo determination of the force of leucocyte-endothelium adhesion in the mesenteric microcirculature of the cat. *Circ. Res.* **63**, 658–668.

JOSEPH, D. D. 1990 Separation in flowing fluids. *Nature* **348**, 487.

JOSEPH, D. D., NGUYEN, K. & BEAVERS, G. S. 1984*a* Non-uniqueness and stability of the configuration of flow of immiscible fluids with different viscosities. *J. Fluid Mech.* **141**, 319–345.

JOSEPH, D. D., RENARDY, M. & RENARDY, Y. 1984*b* Instability of the flow of two immiscible liquids with different viscosities in a pipe. *J. Fluid Mech.* **141**, 309–317.

LIPOWSKY, H. H., USAMI, S. & CHIEN, S. 1980 In vivo measurements of 'Apparent Viscosity' and microvessel haematocrit in the mesentery of the cat. *Microvasc. Res.* **19**, 297–319.

MACLEAN, D. L. 1973 A theoretical analysis of bicomponent flow and the problem of interface shape. *Trans. Soc. Rheol.* **17**, 385–399.

MARSHALL, J. M. 1991 The venous vessels within skeletal muscle. *News in Physiol. Sci.* **6**, 11–15.

OUDE EGBRINK, M. G. A., TANGELDER, G. J., SLAAF, D. W. & RENEMAN, R. S. 1991 Fluid dynamics and the thromboembolic reaction in mesenteric arterioles and venules. *Am. J. Physiol.* **260**, H1826–H1833.

PRIES, A. R., LEY, K., CLASSEN, M. & GAEHTGENS, P. 1989 Red cell distribution in microvascular bifurcations. *Microvasc. Res.* **38**, 81–101.

PRIES, A. R., SECOMB, T. W., GAEHTGENS, P. & GROSS, J. F. 1990 Blood flow in microvascular networks: Experiments and simulation. *Circ. Res.* **67**, 826–834.

SATO, M. & OHSHIMA, N. 1989 Effect of wall shear rate on thrombogenesis in microvessels of the rat mesentery. *Circ. Res.* **66**, 941–949.

SCHMID-SCHÖNBEIN, G. W., SKALAK, R., USAMI, S. & CHIEN, S. 1980 Cell distribution in capillary networks. *Microvasc. Res.* **9**, 18–44.

SCHMID-SCHÖNBEIN, G. W. & ZWEIFACH, B. W. 1975 RBC velocity profiles in arteriole and venules of the rabbit omentum. *Microvasc. Res.* **10**, 153–164.

SOUTHERN, J. H. & BALLMAN, R. L. 1973 Stratified bicomponent flow of polymer melts in a tube. *Appl. Polymer Symp.* **20**, 175–189.

STOCKMAN, H. W., STOCKMAN, C. T. & CARRIGAN, C. R. 1990 Modelling viscous segregation in immiscible fluids using lattice-gas automata. *Nature* **348**, 523–525.

TANGELDER, J. G., TEIRLINCK, H. C., SLAAF, D. W. & RENEMAN, R. S. 1985 Distribution of blood platelets flowing in arterioles. *Am. J. Physiol.* **248**, H318–H323.

TUTTY, O. R. 1988 Flow in a tube with a small side branch. *J. Fluid Mech.* **191**, 79–109.

WHITE, J. L. & LEE, B. L. 1975 Theory of interface distortion in stratified two-phase flow. *Trans. Soc. Rheol.* **19**, 457–479.

WILLIAMS, M. C. 1975 Migration of two liquid phases in capillary extrusion: An energy interpretation. *AIChE J.* **21**, 1204–1207.

YAMAGUCHI, S., YAMAKAWA, T. & NIIMI, H. 1992 Cell-free layer in cerebral microvessels. *Biorheology* **29**, 251–260.

YAN, Z., ACRIVOS, A. & WEINBAUM, S. 1991 Fluid skimming and particle entrainment into a small circular side pore. *J. Fluid Mech.* **229**, 1–27.